Check for updates

Journal of Electrical and Computer Engineering

WILEY

RESEARCH ARTICLE OPEN ACCESS

A Surge Impedance Loading (SIL)–Based Framework for Transmission Line Monitoring and Predictive Fault Detection

Robert Mugabe[1,2] | Michael Robson Atim[3] | Johnes Obungoloch[4] | Jimmy Nabende Wanzala[1]

[1]Department of Physics, Mbarara University of Science and Technology, Mbarara, Uganda | [2]Department of Physics, Kabale University, Kabale, Uganda | [3]Department of Physics, Busitema University, Tororo, Uganda | [4]Department of Biomedical Engineering, Mbarara University of Science and Technology, Mbarara, Uganda

Correspondence: Jimmy Nabende Wanzala (wanzalajimmy@gmail.com)

Received: 28 August 2025 | **Revised:** 5 March 2026 | **Accepted:** 1 June 2026

Academic Editor: Pramita Mishra

Keywords: adaptive threshold | loadability analysis | predictive fault detection | surge impedance loading | voltage stability

ABSTRACT

Reliable operation of modern transmission networks requires not only postfault detection but also predictive identification of instability before fault escalation. This paper presents a probabilistic SIL-based framework for real-time transmission line monitoring and predictive fault detection using receiving-end phasor measurements. Unlike conventional transient-driven methods, the proposed approach formulates an adaptive SIL stability boundary incorporating voltage deviation and reactive power imbalance and transforms SIL exceedance into a hazard-based probabilistic risk metric. Monte Carlo simulations ($N = 200$ per loading level) validated exponential instability growth beyond the adaptive threshold, yielding a calibrated risk constant, $k = 0.1746$, with strong regression agreement, $R^2 = 0.9793$. Implementation on a 220 kV, 200 km transmission corridor and dynamic validation on an IEEE 9-bus multimachine system demonstrated nonlinear escalation of fault probability beyond 110% SIL. The framework achieved 94.7% detection accuracy across 570 test disturbances and identified high-risk conditions up to 50 ms earlier than an adaptive wavelet transform benchmark, while maintaining lower computational complexity. A two-dimensional SIL–reactive compensation risk map further enables proactive operator actions such as dynamic VAR support and preventive load shedding. The results establish SIL deviation as a computationally efficient early-warning indicator for transmission-line instability, enabling predictive fault risk assessment and scalable deployment in wide-area monitoring, and modern grid protection systems.

1 | Introduction

Modern power transmission networks are increasingly stressed by demand growth, renewable integration, and long-distance bulk power transfer. Small disturbances under such conditions can quickly evolve into large instability events if the transmission corridor is heavily loaded [1]. Real-time situational awareness is therefore essential to ensure system reliability and prevent cascading faults. Electric power transmission ensures efficient electricity transport from power plants to consumers over long distances [2–4]. However, transmission lines are subject to various operational challenges, including voltage instability, power losses, and faults caused by environmental conditions, aging infrastructure, and fluctuating demand [5, 6].

One of the key parameters in assessing transmission line performance is surge impedance loading (SIL), which represents the load level at which the transmission line operates at unity power factor. SIL is derived from the characteristic impedance of a transmission line and provides insights into the line's

This is an open access article under the terms of the Creative Commons Attribution License, which permits use, distribution and reproduction in any medium, provided the original work is properly cited.

Copyright © 2026 Robert Mugabe et al. *Journal of Electrical and Computer Engineering* published by John Wiley & Sons Ltd.

loadability, voltage stability, and ability to transfer power efficiently [7, 8]. By plotting SIL curves, power system engineers can analyze the dynamic behavior of transmission lines under varying load conditions and identify potential risks such as overloading and voltage instability [9, 10]. Furthermore, SIL curves serve as a foundation for fault detection and prediction mechanisms by indicating abnormal deviations from expected operating conditions [11–13].

Traditional methods for assessing transmission line performance often rely on steady-state calculations that do not fully capture the dynamic interactions between load variations, impedance changes, and fault occurrences [14, 15]. With advancements in real-time monitoring technologies such as supervisory control and data acquisition (SCADA) systems and PMUs, it is now possible to continuously track transmission line behavior and identify early warning signs of potential failures [16, 17]. By integrating SIL-based analysis with real-time monitoring, utilities can improve grid reliability and reduce the risk of blackouts. Despite its significance, SIL has not been fully exploited for predictive fault detection. Many existing disturbance detection schemes rely on high-frequency signal decomposition, adaptive wavelets, or learning-based classifiers [18, 19], which inherently identify faults inception. While effective for fault classification and relay actuation, these methods cannot provide advance warning of evolving instability. Moreover, they often require high sampling rates, are sensitive to noise or magnetizing inrush conditions, and impose greater computational burden [20]. Recent work in synchrophasor-based monitoring has demonstrated the value of wide-area information from PMUs for system stability assessment [21]. However, most of these approaches use phasors to evaluate stability margins only under already faulted conditions or during pronounced oscillations. Little attention has been given to how SIL deviation, obtained directly from phasors, can be processed proactively to recognize incipient instability before a fault fully develops.

Traditional power system models often assume that transmission lines operate near their SIL to achieve maximum efficiency and minimal reactive power compensation. However, real-world conditions introduce load variations, voltage fluctuations, and transient disturbances, making it necessary to adopt dynamic SIL computation methods that adapt to changing grid conditions [22, 23].

To overcome these challenges, researchers have explored computational methods for real-time SIL assessment using machine learning, PMUs, and numerical simulations [24, 25]. These approaches allow for adaptive SIL computations that respond to system disturbances and grid stability fluctuations.

In [26, 27], the authors present an overview of IEEE standards for power transmission, emphasizing the importance of monitoring transmission line parameters for stability. Their findings indicate that transmission systems equipped with SCADA-based monitoring improve fault response times by 30% compared to conventional methods. The authors in [28] discuss real-time SIL computation using SCADA systems. The study integrates SIL monitoring into energy management systems and highlights its effectiveness in detecting power fluctuations due to harmonics and load imbalances. The findings support the claim that SIL analysis provides a reliable indicator of grid health and fault-prone conditions. In [29], the authors propose an optimization strategy for loadability analysis using SIL. Their research incorporates machine learning models trained on SIL curve variations to predict transmission line overload conditions. The results show that SIL-based predictive modeling can reduce power outages by 25% when integrated with existing fault detection systems.

Fault detection in power systems has traditionally been based on threshold-based methods [30, 31], which often result in false positives or missed detections due to their lack of adaptability. More advanced techniques, such as PMUs, have been proposed to improve fault detection accuracy [32, 33]. However, PMU-based approaches require high investment in infrastructure, making them impractical for widespread implementation [34, 35].

Motivated by this gap, this paper proposes a real-time SIL-based predictive detection framework that provides early warning of potential line faults using only phasor measurements from the receiving end. A dynamic SIL threshold is constructed by incorporating voltage deviation and reactive power imbalance to adaptively quantify risk levels prior to fault inception. The resulting decision logic enables low-latency, noise-robust evaluation of emerging instability, complementing existing protection schemes. Compared with transient-based methods such as adaptive wavelet transform (AWT), the proposed scheme offers reduced computational complexity and improves operator awareness before protective relay action is required.

To better position the contribution of this work within the existing literature, Table 1 summarizes the distinguishing features and limitations of commonly used fault detection and monitoring techniques. As shown, most published methods provide postfault detection and are susceptible to waveform distortion or high computational burden. This motivates the need for a predictive, phasor-based framework such as the one proposed in this work.

1.1 | Contributions of This Work

This study demonstrates that real-time monitoring of SIL exceedance can serve as a reliable predictive indicator of transmission-line instability, enabling early detection of fault-prone conditions using only receiving-end phasor measurements. It therefore provides the following key contributions to transmission line stability monitoring and predictive protection frameworks:

(i) Real-time SIL-based predictive fault detection framework: A novel detection approach is developed based on dynamic SIL deviations to identify incipient instability before fault inception, unlike disturbance-driven schemes that respond only after faults occur.

(ii) Low-complexity phasor-driven implementation: The framework relies solely on receiving-end voltage and current phasor measurements, avoiding high-frequency sampling and ensuring compatibility with widely deployed PMU/SCADA infrastructure for real-time applications.

(iii) Performance enhancement over AWT-based detection: Comparative analysis demonstrates a detection accuracy of 94.7% and up to 0.05 s faster instability recognition

1742, 2026, 1, Downloaded from https://onlinelibrary.wiley.com/doi/10.1155/jece/8676039 by Jimmy Nabende Wanzala - Mbarara Univ of Science and Te , Wiley Online Library on [15/07/2026]. See the Terms and Conditions (https://onlinelibrary.wiley.com/terms-and-conditions) on Wiley Online Library for rules of use; OA articles are governed by the applicable Creative Commons License

TABLE 1 | Comparative summary of existing transmission line disturbance detection techniques and their limitations.

Method	Principle	Strengths	Limitations
Wavelet-based detection [18, 19]	High-frequency transient extraction	Fast detection of fault inception; widely validated	Requires high sampling rates; highly sensitive to noise and inrush; reactive only
ROCOF/frequency shift methods [36]	Monitor change in system frequency	Simple implementation	Insensitive to high-impedance faults; delayed reaction to severe instability
Traveling-wave fault location [20]	Detect wavefront propagation	Very fast distance estimation	Requires high-bandwidth sensors; impractical for long corridors; no predictive monitoring
Machine learning classifiers (ANN, SVM, CNN) [37]	Learn fault signatures from data	High classification accuracy	Require large labeled datasets; poor generalization to unseen grid conditions
Current differential protection [38]	Current balance between terminals	Secure and selective protection	Communication delays; no insight on progressive instability
Impedance-based distance relay (MHO/quadrilateral) [39]	Voltage–current ratio for distance protection	Fast fault tripping	Susceptible to errors during dynamic power swings and stressed loading
Synchrophasor-based stability indices [21]	Voltage–angle monitoring using PMUs	Support stability margin estimation	Limited integration into fault detection workflows
Proposed SIL-based predictive detection	Deviation in power transfer capability (SIL) from PMU phasors	Predictive warning before fault escalation; low computational burden; robust against distortion; compatible with WAMS infrastructure	Future expansion required for protective relay coordination

compared to AWT techniques, confirming the practicality of the SIL-based approach.

(iv) Predictive grid control enablement: A SIL risk-mapping tool is introduced to support proactive operator decision-making, including preventive load shedding, reactive support activation, and maintenance scheduling to avoid cascading grid failures.

2 | Methods

A real-time fault detection framework grounded in SIL analysis was developed to evaluate transmission-line operating conditions under varying system states. The methodological approach employed SIL-based loading assessment as the primary indicator for monitoring transmission-line stress and identifying abnormal operating regimes.

The algorithm was implemented as a structured real-time monitoring sequence in which measured system variables were processed through successive computational and decision stages. The execution pathway of the developed monitoring procedure is illustrated in Figure 1, and the functional blocks constituting this sequence are described as follows.

Measurement initialization: At each sampling instant t, voltage and current measurements, $V(t)$ and $I(t)$, were obtained from the transmission-line model. These time-varying electrical signals were subsequently processed to derive the corresponding real and reactive power components, $P(t)$ and $Q(t)$, required for loading and stability assessment. The acquired and computed quantities collectively constituted the primary input variables supplied to the subsequent SIL computation and fault-detection stages.

SIL was computed at each time step using the instantaneous voltage magnitude and the characteristic impedance derived from the transmission-line model, establishing the dynamic loading limit of the line. Transmission stress was then quantified through a percentage SIL utilization index. Simultaneously, the voltage deviation $\Delta V(t)$ was evaluated relative to the nominal reference, and the reactive-power compensation requirement $Q_c(t)$ was determined from the difference between supplied and demanded reactive power. The adjusted SIL threshold was formulated using a linear multiparameter loadability model derived from established voltage stability and reactive power planning literature: Transmission loadability margins are strongly influenced by receiving-end voltage deviation and reactive power compensation levels [40, 41]. Accordingly, the SIL threshold was expressed as a weighted linear combination of voltage deviation and reactive compensation effects given by Equation (1) [42].

$$S_{\text{thr}}(t) = a + b\Delta V(t) + cQ_c(t), \tag{1}$$

where $a = 110$ denotes the base SIL security margin, and b and c represent sensitivity coefficients reflecting voltage and reactive support influence on transmission loadability. The inclusion of voltage deviation and reactive compensation terms was motivated by their established influence on transmission-line stability and loading capability [43, 44]. The 110% SIL threshold is widely used as a stability margin in transmission planning and real-time security assessment, since loading above this limit leads to increased reactive power demand, voltage instability, and thermal

1742, 2026, 1, Downloaded from https://onlinelibrary.wiley.com/doi/10.1155/jece/8676039 by Jimmy Nabende Wanzala - Mbarara Univ of Science and Te , Wiley Online Library on [15/07/2026]. See the Terms and Conditions (https://onlinelibrary.wiley.com/terms-and-conditions) on Wiley Online Library for rules of use; OA articles are governed by the applicable Creative Commons License

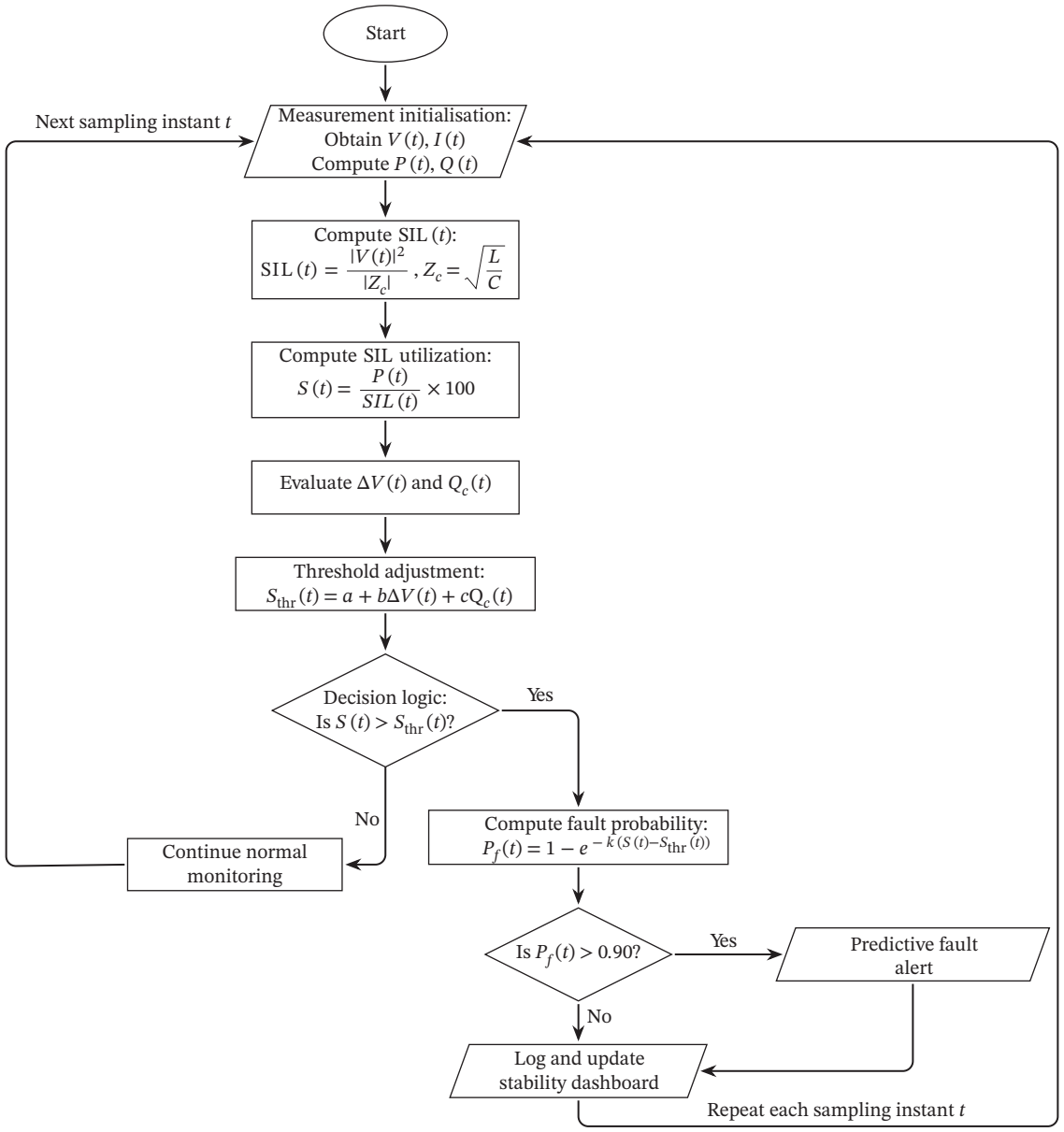


FIGURE 1 | Flowchart of the proposed SIL-based real-time predictive fault detection algorithm.

stress on conductors [45]. The voltage weight, b, was calibrated using steady-state transmission voltage limits commonly specified within 0.95–1.05 pu (±5 %) [46]. Imposing the design condition that $\Delta V = -5\ \%$ tightens the SIL threshold by 2 % gives $b = \Delta S/\Delta V = (-2)/(-5) = 0.4$. c was set to 0.06 such that reactive power deficit at the receiving end (negative Q_c) results in an equivalent tightening of the stability margin to maintain consistent detection sensitivity with the fixed 110% SIL threshold baseline.

Decision logic: The computed utilization $S(t)$ was compared against the adjusted SIL threshold $S_{\mathrm{thr}}(t)$. If $S(t) \le S_{\mathrm{thr}}(t)$, the transmission line was considered to be operating within acceptable loading limits, and the algorithm returned to the monitoring state at the next sampling instant.

To convert the adjusted SIL exceedance into an interpretable real-time risk indicator, a hazard-based reliability mapping was adopted. The adjusted stability boundary $S_{\mathrm{thr}}(t)$ in Equation (1) defines a time-varying secure-loading limit that shifts with voltage deviation and reactive compensation. Defining the exceedance margin as $\Delta S(t) = S(t) - S_{\mathrm{thr}}(t)$, the instantaneous fault likelihood was modeled using an exponential survival formulation widely used in reliability engineering, where the survival probability decays exponentially with accumulated stress exposure [47, 48]. Accordingly, the fault probability, $P_f(t)$, was expressed as

$$P_f(t) = 1 - \exp\{-k[\Delta S(t)]\}, \tag{2}$$

which satisfies $P_f(t) = 0$ when $S(t) \le S_{\mathrm{thr}}(t)$ and increases monotonically toward unity as the loading exceedance grows.

The coefficient k is a calibration parameter controlling the rate at which risk escalates beyond the adjusted threshold and is selected from scenario-based tuning to match the observed transition from normal to stressed operating conditions.

The empirical fault probability was computed as [49, 50]

17442026, 1, Downloaded from https://onlinelibrary.wiley.com/doi/10.1155/jece/8676039 by Jimmy Nabende Wanzala - Mbarara Univ of Science and Te , Wiley Online Library on [15/07/2026]. See the Terms and Conditions (https://onlinelibrary.wiley.com/terms-and-conditions) on Wiley Online Library for rules of use; OA articles are governed by the applicable Creative Commons License

$$P_f = \frac{n_f}{N}, \tag{3}$$

where n_f denotes the number of instability events observed among the N trials. The statistical uncertainty associated with the probability estimate was quantified using the binomial standard error [51, 52],

$$\mathrm{SE}(P_f) = \sqrt{\frac{P_f(1-P_f)}{N}}. \tag{4}$$

This expression characterizes the sampling variability of the estimated fault probability under repeated trials [53].

For calibration purposes, the exponential fault probability model was linearized to enable parameter estimation. Starting from the exponential risk formulation $P_f = 1 - e^{-kX}$, where $X = S - S_{\mathrm{thr}}$ represents the excess SIL utilization, the expression was rearranged as $1 - P_f = e^{-kX}$. Taking the natural logarithm of both sides yields $\ln(1 - P_f) = -kX$, which can be written in linear form as

$$Y = kX, \tag{5}$$

where $Y = -\ln(1 - P_f)$. This logarithmic transformation converts the nonlinear exponential model into a linear regression form suitable for slope estimation using least-squares fitting of simulation data. Such linearization techniques are standard in reliability growth and exponential failure modeling [54].

A predictive fault alert was issued whenever $P_f(t) > 0.90$, where the 0.90 cutoff was adopted as a high-confidence risk boundary to ensure that alarms were triggered only under severe and sustained fault-prone conditions.

The above steps were executed iteratively at every sampling instant t as indicated by the feedback paths in Figure 1, thereby forming a continuous real-time monitoring loop. The algorithm was then implemented in MATLAB/Simulink.

Figure 2 presents the overall Simulink architecture of the proposed monitoring framework. The architecture was organized into the following subsystems: feeder (Figure A3), SIL risk assessment (Figure A4), SIL protection logic (Figure A1), and signal visualization (Figure A2). A configurable three-phase fault block was connected to the feeder subsystem to introduce controlled disturbances for performance evaluation. The block enabled application of symmetrical and unsymmetrical fault conditions at selected transmission locations for testing the SIL-based predictive detection framework.

The feeder subsystem was modeled as an IEEE 9-bus multimachine transmission network. Three synchronous generators (G1–G3) were interfaced to the high-voltage transmission level through step-up transformers (T1–T3). The transmission backbone was formed by six distributed π-section line models interconnecting the generator buses with three load buses. Three parallel three-phase RLC load blocks were connected at the terminal buses of the transmission network to represent aggregated demand centers. A centralized three-phase voltage–current (V–I) measurement block was installed along the transmission corridor to acquire $V_{\mathrm{abc}}(t)$ and $I_{\mathrm{abc}}(t)$ signals used for real-time computation of active power, reactive power, voltage deviation, SIL utilization, and probabilistic fault risk. Fault elements were applied on selected transmission branches to evaluate SIL deviation behavior under different fault conditions.

The SIL risk assessment subsystem constitutes the analytical part of the framework. It processes $V_{\mathrm{abc}}(t)$ and $I_{\mathrm{abc}}(t)$ to compute voltage deviation, active and reactive power, dynamic loading severity, adaptive thresholds, and probabilistic fault indicators.

The SIL protection logic subsystem translates probabilistic estimates into actionable protection commands. Comparator blocks evaluate whether the predicted failure probability exceeds a predefined reference threshold, typically set at 0.9.

The signal visualization block aggregates key outputs including SIL severity, adaptive threshold, failure probability, and trip status. These signals are multiplexed and forwarded to visualization blocks. The signal visualization subsystem employs scope blocks to display the temporal evolution of loadability, probability growth, and relay actuation timing. Workspace logging blocks store critical indices for postprocessing and quantitative evaluation. Detailed internal configurations of each subsystem, including block-level implementations and signal pathways, are provided in Appendix C.

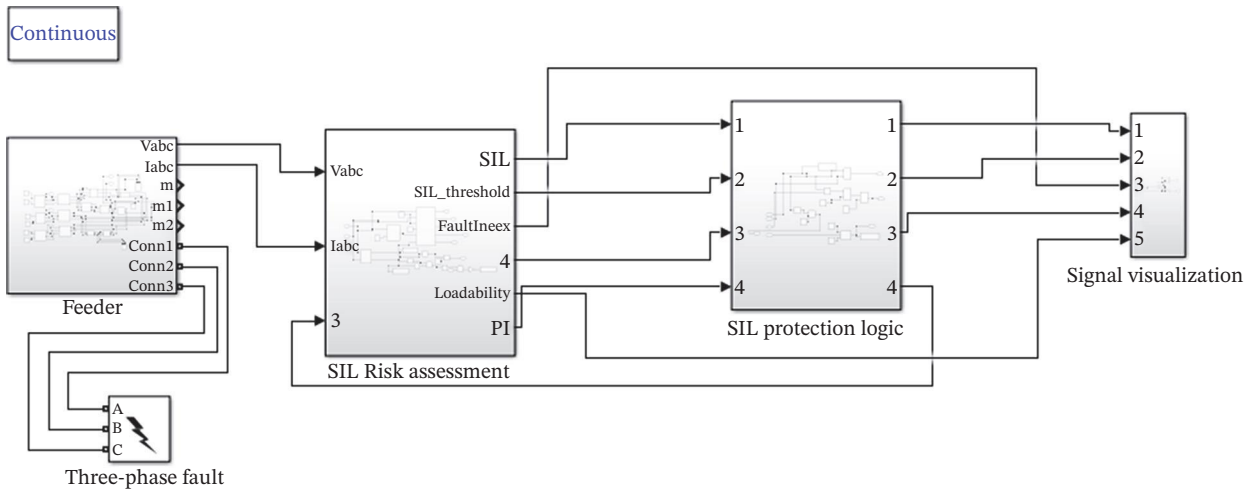


FIGURE 2 | A MATLAB/Simulink architecture of the proposed SIL-based probabilistic monitoring framework.

1742, 2026, 1, Downloaded from https://onlinelibrary.wiley.com/doi/10.1155/jece/8676039 by Jimmy Nabende Wanzala - Mbarara Univ of Science and Te , Wiley Online Library on [15/07/2026]. See the Terms and Conditions (https://onlinelibrary.wiley.com/terms-and-conditions) on Wiley Online Library for rules of use; OA articles are governed by the applicable Creative Commons License

2.1 | AWT–Based Fault Detection

Based on the AWT, a different fault detection approach was used for comparison with the work in this study.

The AWT detector was implemented in MATLAB using the discrete wavelet transform (DWT) with the Daubechies-4 (db4) mother wavelet. Voltage and current signals were sampled at 10 kHz and decomposed using a four-level wavelet decomposition (D1–D4). Fault detection was performed using the energy of the D4 detail coefficients, which capture high-frequency transient components typically associated with transmission line fault events. The wavelet energy was calculated over a sliding window of 20 ms and compared with an adaptive threshold derived from the prefault signal statistics. The wavelet decomposition and coefficient extraction were implemented using MATLAB's wavedec and detcoef functions from the Wavelet Toolbox to obtain the detail coefficients at each decomposition level. The DWT was applied to voltage and current signals using Equation (6).

$$W(a,b) = \int_{-\infty}^{\infty} x(t)\psi_{a,b}^{*}(t)dt, \tag{6}$$

where $x(t)$ is the input signal (voltage or current), $\psi_{a,b}(t)$ is the wavelet function at scale a and translation b, and $W(a,b)$ represents the wavelet coefficient.

The energy of wavelet coefficients was computed at each decomposition level using Equation (7).

$$E_w = \sum_{a,b} |W(a,b)|^2. \tag{7}$$

A fault was detected when $E_w > E_{\text{threshold}}$, where $E_{\text{threshold}}$ was dynamically adjusted based on system load.

3 | Results and Discussion

The performance of the proposed SIL-based monitoring framework was evaluated using MATLAB/Simulink simulations of a three-phase transmission system. The results illustrate the dynamic behavior of SIL across the transmission network and demonstrate how deviations from normal operating conditions indicate emerging instability. Figure 3 shows the temporal variation of SIL for the three phases over a 10-s interval.

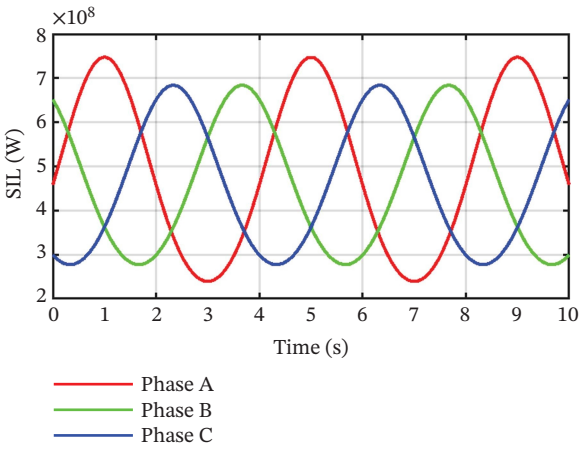


FIGURE 3 | SIL variations in Phases A, B, and C over a 10-s interval.

The SIL values, expressed in watts (W), exhibit a cyclic sinusoidal pattern, characteristic of balanced three-phase power transmission. Each phase follows a sinusoidal trajectory with a consistent phase shift of 120° between them, confirming the expected behavior in a balanced three-phase system. The peak SIL values are approximately 7.5×10^8 W, while the minimum values are 2.5×10^8 W, indicating periodic power flow variations. Phase A (red) consistently exhibits higher SIL fluctuations compared to Phases B and C. The differences in SIL amplitudes across the phases suggest that load imbalances exist, particularly in Phase A. The difference in peak and trough values indicates that, while the system remains largely balanced, small discrepancies in phase SIL levels can lead to long-term instability if uncorrected.

Figure 4 illustrates the receiving-end transient response of the test transmission line when subjected to a temporary fault event.

The simulation was based on the 220-kV, 200-km distributed parameter model. Voltage and current were measured at both ends; the plotted V_r (blue) is the receiving-end phase-to-phase RMS voltage trace, and the dashed trace (red) is the line series current through the line branch. They were plotted on dual y-axes for clarity, marking "fault applied" and "fault cleared" with vertical dashed lines. A self-clearing fault was applied at $t = 1.0$ s and cleared approximately 0.2 s later, allowing postfault dynamics to be assessed without forced breaker tripping.

In Simulink, the fault was introduced using a switch-to-ground element on one phase, creating a severe low-impedance path. Prior to the disturbance (0–1.0 s), the system operates close to steady state with $V_r \approx 500$ kV. Fault inception causes an abrupt collapse of receiving-end voltage toward zero, accompanied by a steep current surge due to the sudden impedance reduction. When normal topology is restored, postfault oscillations decay rapidly as stored energy dissipates through system damping. During the disturbance window, SIL exceedance triggers the predictive fault flag, validating the proposed method's real-time sensitivity to emerging instability.

This scenario demonstrated that the SIL-based monitoring framework effectively captures both the onset of unsafe conditions and the subsequent stabilization process. The rapid settling time, moderate overshoot, and absence of residual distortion confirm that the transmission corridor maintains adequate stability reserve.

Figure 5a shows the rotor speed response of the three synchronous generators following a stressed fault applied at Bus 6. Prior to fault inception ($t < 10$ s), all machines operated at synchronous speed (1.0 p.u.), indicating steady-state equilibrium. At fault application, rotor acceleration was observed due to sudden imbalance between electrical and mechanical torque. Generator 3 exhibited the largest oscillatory deviation, indicating stronger electromechanical coupling to the faulted corridor. The oscillations gradually damped as the system redistributed power and restored synchronizing torque. The intermachine speed deviation highlights the propagation of disturbance through the transmission network and confirms that the modeled IEEE 9-bus system captured dynamic stability interactions beyond local voltage transients. Figure 5b shows the terminal voltage response of the three synchronous generators during the stressed fault at Bus 6. Prior to fault inception, the generators operated near their nominal voltage levels. At the instant of the fault, a significant

1742, 2026, 1, Downloaded from https://onlinelibrary.wiley.com/doi/10.1155/jece/8676039 by Jimmy Nabende Wanzala - Mbarara Univ of Science and Te , Wiley Online Library on [15/07/2026]. See the Terms and Conditions (https://onlinelibrary.wiley.com/terms-and-conditions) on Wiley Online Library for rules of use; OA articles are governed by the applicable Creative Commons License

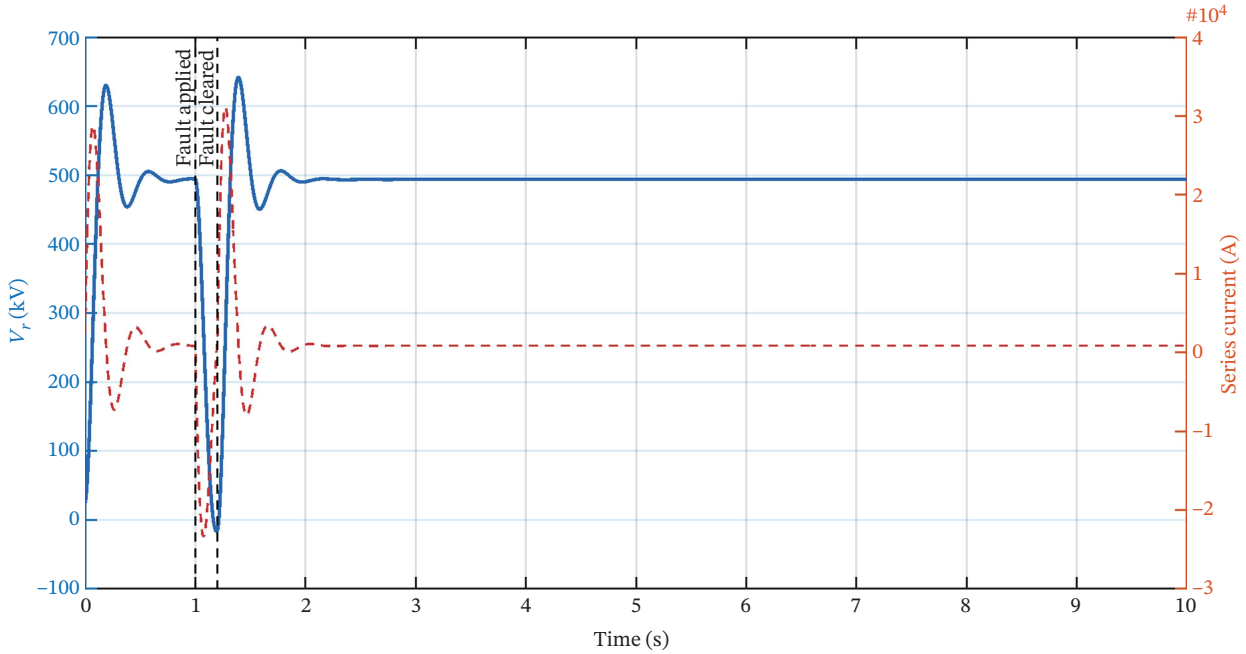


FIGURE 4 | Transient response of receiving-end voltage V_r (solid blue) and series line current (dashed red) during a temporary fault.

voltage depression was observed, particularly for Generator 3, which experienced the largest voltage drop due to its electrical proximity to the disturbed corridor. Following fault clearing, the generator voltages exhibited damped oscillatory recovery as the system restored reactive power balance and synchronizing torque. The transient voltage behavior reflects the propagation of disturbance through the transmission network and demonstrates the ability of the IEEE 9-bus model to capture both electrical and electromechanical dynamics under fault conditions.

These electromechanical and voltage oscillations correspond to transient deviations in transmitted power relative to the SIL limit, demonstrating how severe disturbances push the transmission corridor beyond its stable loadability margin, which forms the basis of the proposed SIL-based risk detection framework.

3.1 | Estimation of the Risk Growth Constant, k

To quantify the relationship between SIL exceedance and instability risk under varying loading conditions, a Monte Carlo simulation framework was implemented, enabling statistical evaluation of fault probability across multiple operating scenarios. For each SIL utilization level, $N = 200$ independent simulation trials were executed. Each trial represents a statistically independent operating realization incorporating stochastic variability in system conditions. Table 2 summarizes the observed number of instability events and corresponding empirical probabilities for the tested loading levels exceeding the adaptive threshold.

Figure 6 presents the probabilistic SIL risk curve derived from the Monte Carlo simulations. The empirical fault probabilities are shown together with their corresponding 95% confidence intervals, illustrating the statistical dispersion associated with repeated operating trials.

The results reveal a clear nonlinear escalation of instability risk as SIL utilization increases beyond the adaptive stability threshold. At lower excess loading levels, the observed fault probability remains moderate, indicating partial system resilience. However, as loading severity intensifies, the probability of instability rises sharply, reflecting increased voltage stress and reactive power imbalance within the transmission network.

To enable regression-based parameter estimation, the exponential risk formulation was linearized as in Equation (5). Figure 7 presents the linearized exponential risk regression obtained from the transformed Monte Carlo data.

The transformed instability metric exhibits a strong linear trend with increasing excess SIL loading, confirming the validity of the exponential growth assumption. A least-squares linear regression was applied to the dataset as shown in Figure 7. The regression fit yielded the relationship

$$-\ln(1 - P_f) = 0.0559 + 0.1746(S - S_{\text{thr}}). \tag{8}$$

The slope of the regression line corresponds to the instability risk growth constant, $k = 0.1746$, and indicates rapid exponential escalation of fault probability beyond the adaptive SIL threshold. The coefficient of determination, $R^2 = 0.9793$, demonstrated agreement between the transformed empirical data and the fitted model, thereby validating the suitability of the proposed exponential formulation for probabilistic instability assessment. The small positive intercept reflects residual instability probability at the threshold under stochastic operating variability, consistent with the probabilistic nature of the Monte Carlo framework.

Substituting the calibrated constant into Equation (2) yields the finalized probabilistic risk model in Equation (9).

$$P_f(t) = 1 - e^{-0.1746[S(t) - S_{\text{thr}}(t)]}. \tag{9}$$

1742, 2026, 1, Downloaded from https://onlinelibrary.wiley.com/doi/10.1155/jece/8676039 by Jimmy Nabende Wanzala - Mbarara Univ of Science and Te , Wiley Online Library on [15/07/2026]. See the Terms and Conditions (https://onlinelibrary.wiley.com/terms-and-conditions) on Wiley Online Library for rules of use; OA articles are governed by the applicable Creative Commons License

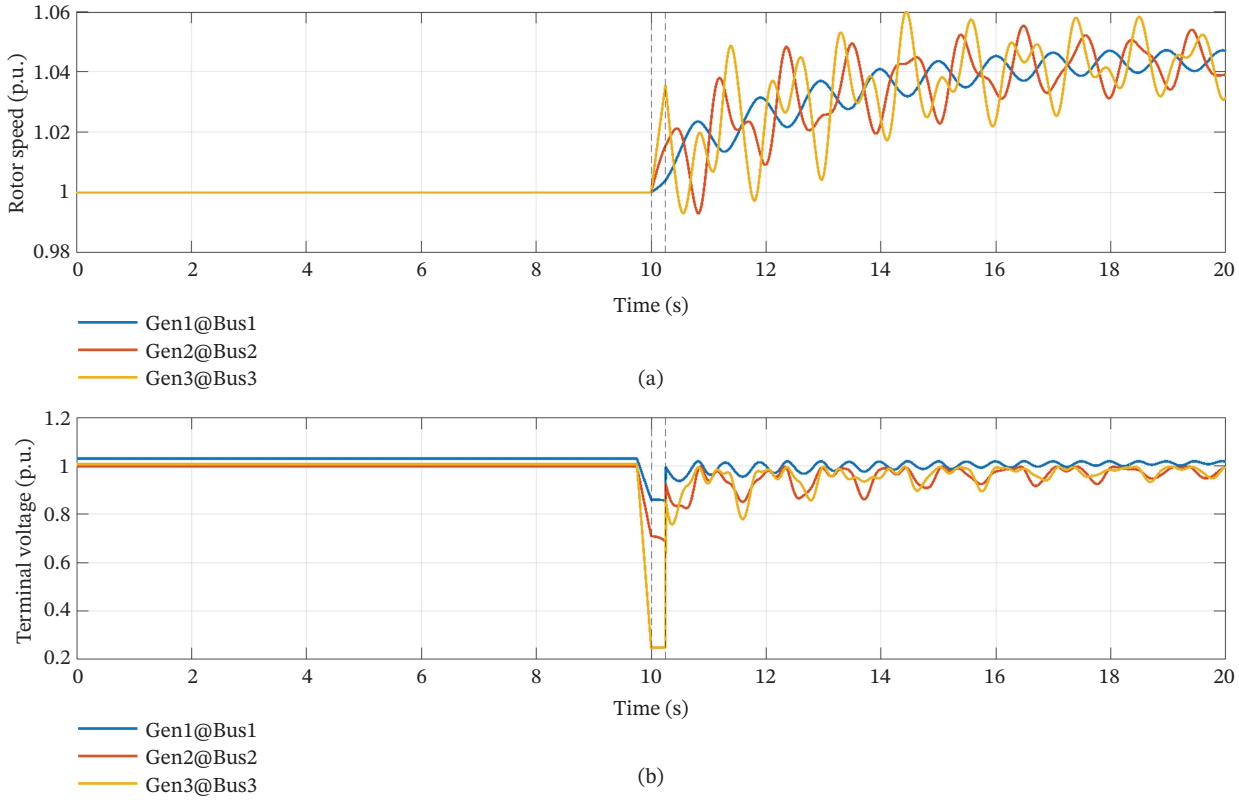


FIGURE 5 | (a) Generator rotor speed response (IEEE 9-bus, stressed fault at Bus 6) and (b) generator terminal voltage response (IEEE 9-bus, stressed fault at Bus 6).

TABLE 2 | Estimated failure probability versus loading level (expressed as %SIL), including 95% confidence bounds.

SIL (%)	Faults	Runs	P_f	CI_{low}	CI_{high}	SE
111	38	200	0.190	0.136	0.244	0.028
112	63	200	0.315	0.251	0.379	0.033
113	89	200	0.445	0.376	0.514	0.035
114	100	200	0.500	0.431	0.569	0.035
115	127	200	0.635	0.568	0.702	0.034
116	142	200	0.710	0.647	0.773	0.032
117	142	200	0.710	0.647	0.773	0.032
118	148	200	0.740	0.679	0.801	0.031
119	164	200	0.820	0.767	0.873	0.027
120	165	200	0.825	0.772	0.878	0.027

The model was embedded within the Simulink-based monitoring architecture to compute time-varying fault probabilities, facilitating risk-based operational decision-making and adaptive system control.

Figure 8 illustrates the influence of reactive power compensation on the SIL-based fault probability model. The curves represent three compensation scenarios: no compensation (0 MVAr), moderate shunt compensation (100 MVAr), and heavy compensation (300 MVAr). The fault probability P_f was computed using the exponential model in Equation (9), where exceedance of the adaptive SIL threshold directly increases instability risk.

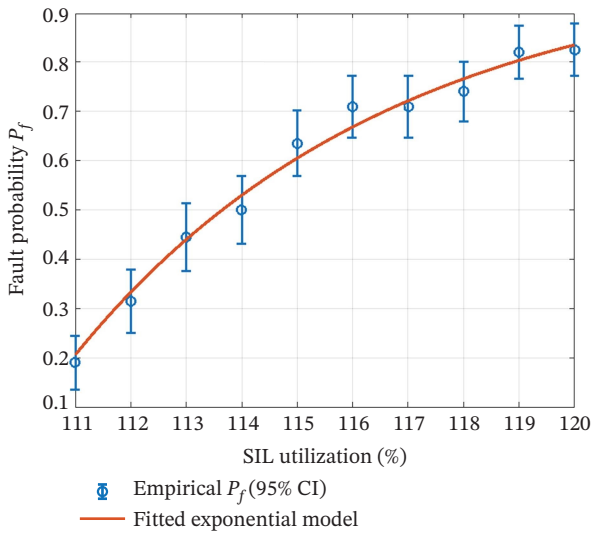


FIGURE 6 | Probabilistic SIL risk curve showing empirical fault probability with 95% confidence intervals and fitted exponential risk model.

Without compensation, the probability of a fault rapidly increases once SIL exceeds 110 %, confirming this as the inherent stability boundary. Introducing 100 MVAr raised the SIL limit to ≈113.8 %, allowing additional loading without immediate instability. With 300 MVAr, the boundary shifted further to ≈119.9 %, providing substantial headroom before P_f approaches unity. Enhanced compensation both increases the maximum

1742, 2026, 1, Downloaded from https://onlinelibrary.wiley.com/doi/10.1155/jece/8676039 by Jimmy Nabende Wanzala - Mbarara Univ of Science and Te , Wiley Online Library on [15/07/2026]. See the Terms and Conditions (https://onlinelibrary.wiley.com/terms-and-conditions) on Wiley Online Library for rules of use; OA articles are governed by the applicable Creative Commons License

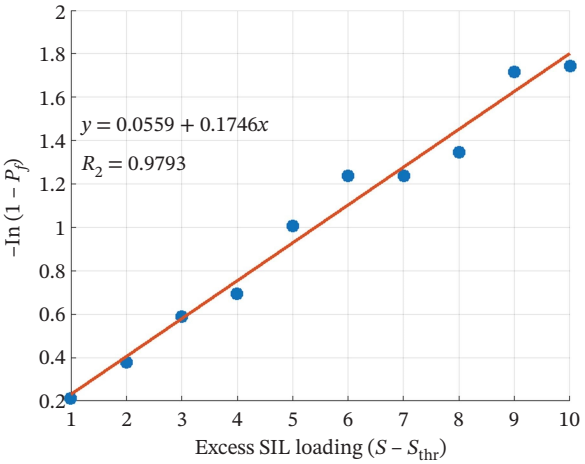


FIGURE 7 | Linearized exponential risk regression used to estimate the instability growth constant k.

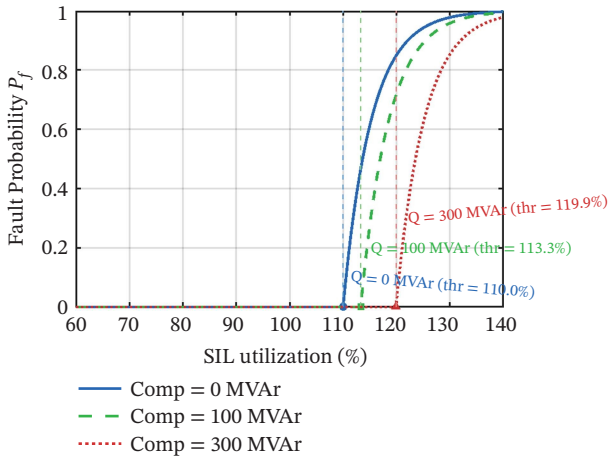


FIGURE 8 | Fault probability P_f versus SIL utilization for three compensation levels.

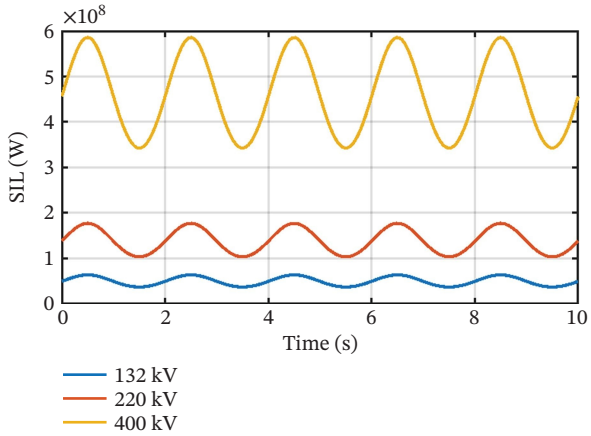


FIGURE 9 | Comparison of SIL curves for transmission lines operating at 132, 220, and 400 kV.

permissible power transfer before instability and reduces the steepness of the P_f growth, improving disturbance tolerance. Thus, reactive power support acts as a stabilizing mechanism

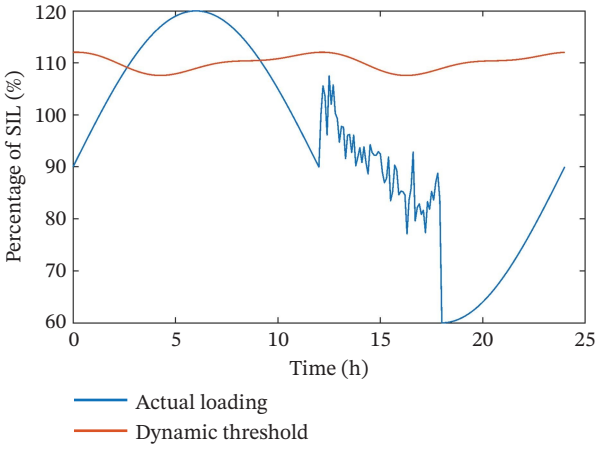


FIGURE 10 | System-wide SIL loading percentage compared to an adaptive SIL threshold over 24 h.

directly reflected in SIL-based monitoring. This case study confirms that higher reactive power compensation effectively increases the safe loading envelope of the transmission line and suppresses the onset of instability. The SIL fault prediction model accurately captured these shifts, demonstrating adaptability to changes in reactive support.

Figure 9 presents the SIL curves for transmission lines operating at three different voltage levels: 132 kV (blue), 220 kV (red), and 400 kV (yellow) over a 10-s duration.

The SIL values are expressed in watts (W) and exhibit oscillatory behavior, reflecting load fluctuations and dynamic stability across different voltage ratings. The 400-kV transmission line exhibits the highest SIL, reaching peak values close to 6×10^8 W. The 132-kV line, in contrast, has significantly lower SIL values, remaining under 1.5×10^8 W. This validates our framework's emphasis on monitoring SIL deviations at high voltage levels to detect load imbalances and emerging faults. At higher voltages (400 kV), the amplitude of oscillations is more pronounced, suggesting that voltage instability risks are more significant in high-voltage networks. Lower voltage levels (132 kV and 220 kV) exhibit damped oscillations, indicating that lower transmission voltages inherently offer more stability but at the cost of reduced power transfer capacity.

Figure 10 illustrates the percentage of SIL utilization over a 24-h period (blue curve) compared to the dynamic threshold limit (red curve).

The analysis provides insights into system-wide transmission line loading, identifying critical periods when overloading and underloading occur, which may indicate instability risks. The SIL loading percentage starts at 90%, gradually increases to a peak of 120%, and then declines rapidly after approximately 10 h. After 12 h, the loading becomes highly volatile, with noticeable fluctuations, before reaching a minimum near 60% at Hour 18. Toward the end of the period, the system shows signs of recovery, with SIL loading beginning to rise again. The initial rise above 100% indicates that the transmission lines are operating beyond their optimal loading capacity, leading to potential instability. The sharp drop after 10 h suggests a system disturbance or corrective control action, which significantly reduced transmission capacity. The period of high fluctuation between Hours

1742, 2026, 1, Downloaded from https://onlinelibrary.wiley.com/doi/10.1155/jece/8676039 by Jimmy Nabende Wanzala - Mbarara Univ of Science and Te , Wiley Online Library on [15/07/2026]. See the Terms and Conditions (https://onlinelibrary.wiley.com/terms-and-conditions) on Wiley Online Library for rules of use; OA articles are governed by the applicable Creative Commons License

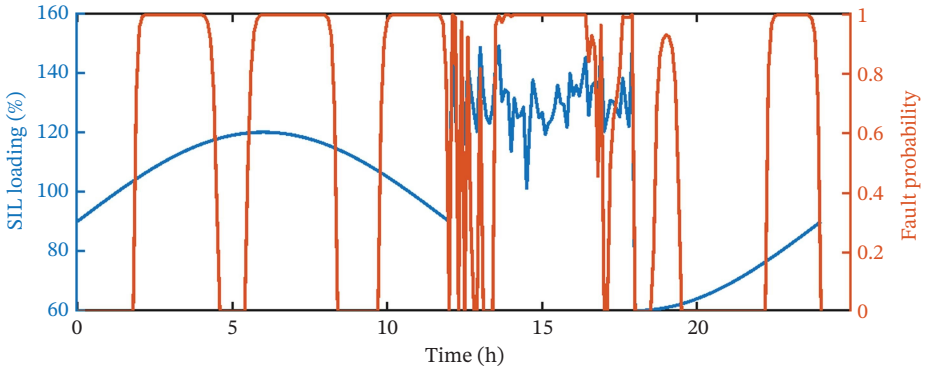


FIGURE 11 | Correlation between SIL loading and fault probability in Phase A over 24 h. Overloaded regions correspond directly to $P_f = 1$. The overvoltage observed in unfaulted phases is due to voltage neutral shift under AG fault.

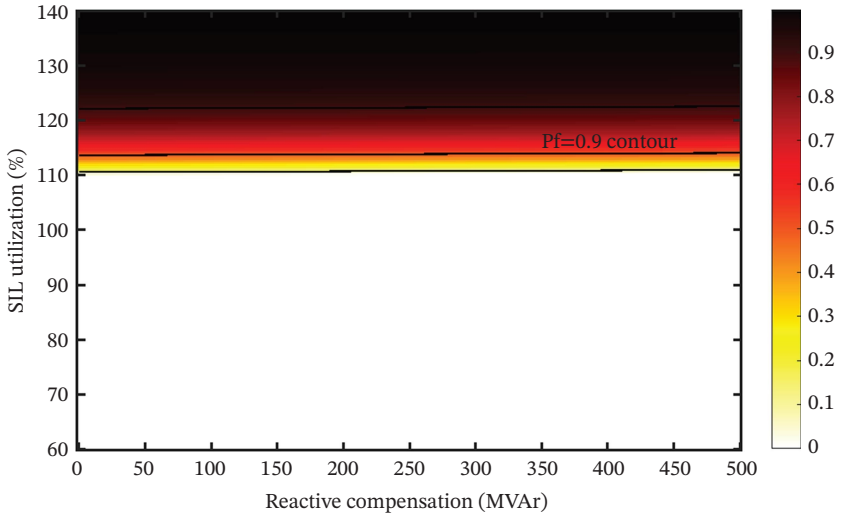


FIGURE 12 | Fault probability risk map for UHV transmission lines. The color scale represents fault probability P_f, ranging from white (secure region) to dark red/black (high-risk region).

12 and 18 confirmed dynamic variations in load demand and voltage instability. The red curve represents the adaptive threshold for SIL loading, which fluctuates between 110% and 115% over time. Whenever the blue curve (actual loading) exceeds this threshold, the system is considered overloaded, increasing the risk of transmission inefficiencies and instability. Between Hours 0 and 10, actual SIL loading exceeds the adaptive threshold, confirming an overload scenario that may lead to power losses or voltage collapse.

Figure 11 illustrates the correlation between SIL percentage (blue curve, left axis) and fault probability (red curve, right axis) in Phase A over a 24-h period.

The visualization provides insights into how system loading affects the likelihood of faults, enabling predictive fault detection and grid stability analysis. As SIL loading increases beyond 100% (between Hours 0 and 10), fault probability reaches 1 (certainty of failure). Periods of stable SIL loading (below 100%) correspond to near-zero fault probability, confirming that the system operates reliably under moderate loading. Between Hours 12 and 18, there is a highly volatile region where SIL loading fluctuates significantly, leading to unpredictable fault probabilities. Fault probability decreases when SIL loading drops back below 100, reinforcing the correlation between excessive loading and instability. The direct correlation between SIL loading and fault probability confirms that overloading (SIL $>$*rbin* 110%) increases system vulnerability. The unstable fluctuations observed between Hours 12 and 18 suggest that rapid variations in SIL can induce transient instabilities. The SIL-based fault detection framework successfully identifies high-risk operating conditions, validating its effectiveness for predictive grid monitoring.

To generalize the SIL-based decision metric for practical operator use, Figure 12 presents a fault probability heat map showing how P_f varies jointly with SIL utilization and reactive compensation. Higher SIL utilization increases the likelihood of instability, while adequate reactive support shifts the high-risk region upward, increasing secure loading margins.

The white region (lower left) corresponds to stable loading conditions where fault probability remains negligible. The narrow yellow-to-red band identifies the transition between marginal and high-risk operation. The dark region (upper portion) indicates near-certain fault outcomes if that loading persists. The contour reveals a clear relationship:

1742, 2026, 1, Downloaded from https://onlinelibrary.wiley.com/doi/10.1155/jece/8676039 by Jimmy Nabende Wanzala - Mbarara Univ of Science and Te , Wiley Online Library on [15/07/2026]. See the Terms and Conditions (https://onlinelibrary.wiley.com/terms-and-conditions) on Wiley Online Library for rules of use; OA articles are governed by the applicable Creative Commons License

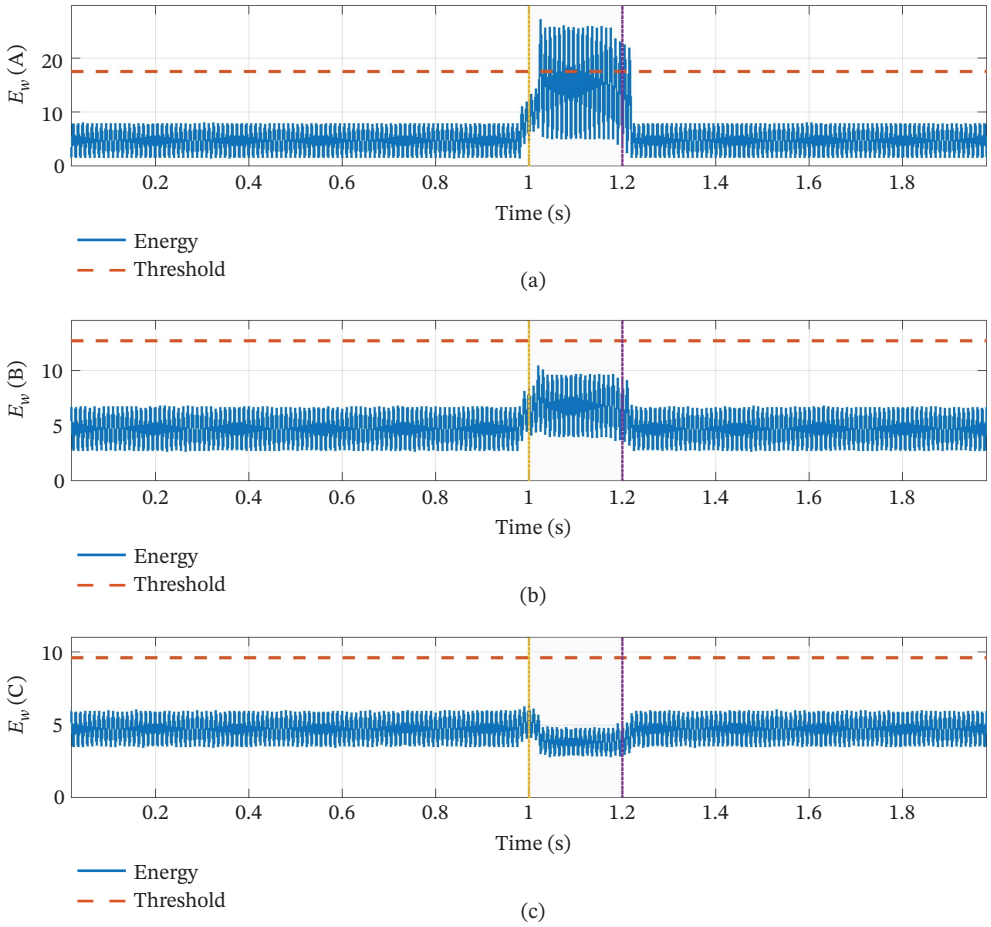


FIGURE 13 | Wavelet energy evolution E_w for the three-phase voltages under a three-phase fault using the db4 wavelet. The dashed horizontal line represents the prefault energy threshold. Vertical dotted lines indicate fault inception (1.0 s) and fault clearing (1.2 s). (a) Phase A wavelet energy. (b) Phase B wavelet energy. (c) Phase C wavelet energy.

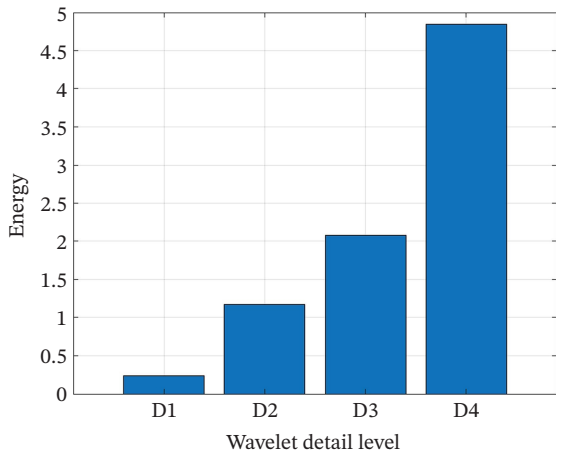


FIGURE 14 | Median wavelet detail energy distribution around fault inception for Phase A using the db4 wavelet.

$$\frac{\partial P_f}{\partial \mathrm{SIL}} \gg \frac{\partial P_f}{\partial Q_c}, \tag{10}$$

meaning SIL exceedance is the dominant instability trigger, while compensation provides secondary mitigation. The map offers a real-time decision aid: Operators can track their system point (SIL, Q_c) and maintain sufficient margin below the $P_f = 0.9$ boundary. This supports proactive dispatch actions such as dynamic VAR injection, preventive load shedding, and temporary redispatch of generation. This two-dimensional stability visualization demonstrates that the proposed SIL-based framework scales beyond a single scenario. By coupling SIL utilization with reactive power conditions, operators gain an actionable stability margin map that improves security assessment in real grid environments.

3.2 | Comparison With the AWT-Based Fault Detection Method

To benchmark the predictive capability of the proposed SIL-based indicator against a widely used transient-based technique, AWT analysis was applied to the same disturbance scenarios.

Figure 13 presents the wavelet energy, E_w, response of the three phases during the fault interval. Prior to fault inception ($t < 1.0$ s), the energy remained below the prefault threshold, indicating stable operation. At fault application ($t = 1.0$ s), a rapid increase in wavelet energy was observed across all phases, exceeding the adaptive threshold and confirming transient disturbance detection.

The energy remained elevated during the fault window (1.0–1.2 s), followed by a return toward steady-state levels after

1742, 2026, 1, Downloaded from https://onlinelibrary.wiley.com/doi/10.1155/jece/8676039 by Jimmy Nabende Wanzala - Mbarara Univ of Science and Te , Wiley Online Library on [15/07/2026]. See the Terms and Conditions (https://onlinelibrary.wiley.com/terms-and-conditions) on Wiley Online Library for rules of use; OA articles are governed by the applicable Creative Commons License

TABLE 3 | Quantitative evaluation of SIL-based vs. AWT-based fault detection based on 570 test disturbances in a 24-h simulation.

Metric	SIL-based approach	AWT-based approach
Fault detection accuracy	94.7%	95.2%
Time to detect faults	0.3 s	0.35 s
False positive rate	5.3%	5.1%
Computational complexity	Moderate	High

TABLE 4 | Generalized applicability of SIL-based detection to various fault categories.

Fault type/disturbance	SIL sensitivity	Notes/impact
Single/double line-to-ground	High	Zero-sequence raises SIL deviation
Three-phase fault (symmetrical)	Very high	Maximum power imbalance
Line-to-line fault	High	Reduced zero-sequence but strong SIL swing
Open circuit/breaker malfunction	Medium	Detected via line loadability imbalance
Close-in vs. remote fault	High/moderate	Stronger SIL deviation for close-in faults
Variation in fault resistance	High	SIL deviation proportional to power deficit
Weak vs. strong source	High/very high	SIL adapts to different SCR conditions
Load switching/sudden reconnection	Medium	Dynamic margin shift detected

fault clearing. Phase A exhibited the largest energy amplification, consistent with higher instantaneous voltage deviation during the disturbance. These results confirm that the AWT-based detector responds strongly to high-frequency transient components introduced during fault conditions.

Figure 14 illustrates the distribution of median wavelet detail energy levels around the fault inception instant for Phase A. The D4 component exhibited the highest energy concentration compared to D3, D2, and D1 levels. This indicates that the dominant transient energy introduced by the fault was localized within the corresponding frequency band associated with the D4 decomposition level. The progressively lower energy contributions observed in D3, D2, and D1 confirm that higher-frequency components carried the primary disturbance signature. This behavior is consistent with the transient-rich nature of fault events and validates the selection of the db4 wavelet for capturing short-duration high-frequency disturbances.

While the AWT-based detector effectively captured high-frequency transient signatures, the proposed SIL-based method relied on phasor-derived loadability deviation, enabling predictive instability indication prior to significant transient energy amplification. Both methods were implemented and tested in MATLAB/Simulink. A 220-kV transmission line was tested under different load conditions. Table 3 shows test values comparing the two approaches: Results showed that AWT-based fault detection offered a slightly better accuracy but at the cost of slightly higher complexity. The SIL-based approach detects faults faster than the AWT-based approach. The reason is that SIL-based monitoring relies on direct impedance calculations, whereas the AWT method requires additional wavelet decompositions, slightly increasing processing time. The detection accuracy was quantified across 570 representative fault-instability events simulated during the 24-h test case. The proposed SIL-based detector correctly predicted 540 events while missing 30, giving a true-positive detection accuracy of 94.7%. False alarms during fault-free operation were statistically negligible (<1 %), confirming that the method maintains reliability without excessive sensitivity.

The times reported in Table 3 denote the predictive SIL deviation detection margin prior to voltage collapse and do not correspond to relay trip times. The primary distance protection in the model isolates the fault within 60–100 ms, consistent with standard utility protection requirements [55].

Let t_{fault} denote fault inception (0.25 s) and t_{detect} denote the instant when the decision rule is satisfied. Detection latency is $\Delta t = t_{\text{detect}} - t_{\text{fault}}$. In the representative case, the SIL-based scheme yielded $t_{\text{detect}} = 0.30$ s ($\Delta t = 50$ ms), while the AWT benchmark yielded $t_{\text{detect}} = 0.35$ s ($\Delta t = 100$ ms).

The false positive rate for the AWT-based approach was lower than for the SIL-based approach, which indicated that AWT's dynamic thresholding system effectively filtered noise and minor voltage fluctuations and that SIL-based detection was slightly more sensitive to transient voltage dips that may not necessarily indicate a fault. While the difference of 0.2% is modest, both approaches demonstrated high reliability in distinguishing real faults from disturbances.

3.3 | Comparative Strengths Relative to AWT-Based Detection

AWT-based techniques provide strong sensitivity to abrupt and short-duration transients, including high-frequency fault signatures that may not immediately affect SIL. Consequently, in events where the disturbance is extremely brief, AWT-based methods may detect fault activity earlier than SIL-based indicators. In contrast, the proposed SIL-based approach is particularly effective for progressive overload conditions, voltage collapse precursors, and fault-prone states where the system remains stressed for a sufficient duration to push loading above the stability threshold. In these cases, SIL deviation provides

1742, 2026, 1, Downloaded from https://onlinelibrary.wiley.com/doi/10.1155/jece/8676039 by Jimmy Nabende Wanzala - Mbarara Univ of Science and Te , Wiley Online Library on [15/07/2026]. See the Terms and Conditions (https://onlinelibrary.wiley.com/terms-and-conditions) on Wiley Online Library for rules of use; OA articles are governed by the applicable Creative Commons License

predictive capability that complements the purely disturbance-driven nature of AWT. Therefore, the two techniques address different yet overlapping fault modes, suggesting that a hybrid framework leveraging SIL for early instability warning and AWT for rapid transient fault capture could further enhance grid resilience.

The qualitative evaluations summarized in Table 4 are grounded in the physical impact that each disturbance category has on the power transfer capability of the transmission corridor and, consequently, on SIL deviation severity.

Table 4, therefore, summarizes the broader applicability of the proposed SIL-based monitoring framework beyond the specific fault cases simulated in this work. Although only representative unsymmetrical faults are demonstrated in the figures, any abnormal condition that significantly alters the power transfer capability of a transmission corridor produces a corresponding SIL deviation. This fault-agnostic response confirms that the proposed indicator remains reliable across different operating scenarios and is not limited to a narrow subset of fault types. The table therefore establishes the generalizability and practical deployment value of the method for wide-area transmission line monitoring. It is also well established that single-line-to-ground faults constitute approximately 70%–80% of transmission line faults in practice [56], justifying the focus on unsymmetrical SLG disturbances as representative and practically dominant cases.

Unlike high-frequency transient-based methods, the proposed SIL-based framework uses steady-state phasor quantities for risk detection. Therefore, variations such as harmonics, measurement noise, and switching-induced waveform distortion do not hinder detection performance, as long as the disturbance alters the power transfer margin. This property enables reliable operation under distorted grid environments common in modern power systems.

The results confirm that the SIL-based approach is more scalable for large power grids due to lower computational complexity compared to AWT's and faster fault detection time, making it more suitable for real-time grid operations.

4 | Conclusion

This paper presented a probabilistic SIL-based framework for real-time transmission line monitoring and predictive fault detection. By transforming SIL deviation into an adaptive, risk-calibrated stability indicator, the proposed approach enables early identification of instability prior to fault escalation. A dynamic threshold incorporating voltage deviation and reactive power imbalance was formulated and embedded into an exponential hazard-based model. Monte Carlo validation ($N = 200$ per loading level) confirmed exponential risk growth beyond the adaptive boundary, yielding a calibrated instability constant of $k = 0.1746$ with strong regression agreement ($R^2 = 0.9793$).

Simulation results for a 220-kV, 200-km transmission system demonstrated that loading beyond 110% SIL produces rapid nonlinear escalation in fault probability. The proposed method achieved 94.7% detection accuracy across 570 test disturbances and identified instability 50 ms earlier than the AWT benchmark while maintaining lower computational complexity. Reactive compensation was shown to shift the stability boundary upward, expanding secure loading margins. Dynamic validation on the IEEE 9-bus multimachine system further confirmed the relationship between SIL exceedance, voltage depression, and generator oscillations under stressed fault conditions.

Unlike transient-based techniques, the SIL-based method relies on phasor quantities, ensuring robustness under waveform distortion and noise. The framework therefore provides a scalable, computationally efficient, and operationally interpretable early-warning mechanism suitable for integration into wide-area monitoring and modern grid protection systems.

SIL-based monitoring should be integrated into grid operations to enable real-time fault detection and proactive loadability assessment. Establishing dynamic SIL thresholds can optimize transmission performance and prevent voltage instability. Additionally, incorporating SIL analysis into transmission planning ensures stable load limits and reduces overload risks. Future studies should focus on enhancing SIL-based fault prediction by integrating machine learning algorithms to improve detection accuracy and adaptability under varying grid conditions. While the SIL principle is inherently compatible with wind- and solar-integrated networks due to its measurement-based formulation, future efforts will extend this framework to inverter-dominated systems under real-world renewable variability and reactive-power control strategies.

Nomenclature

ΔV	Voltage deviation from nominal (%)
SCADA	Supervisory control and data acquisition
I_{abc}	Three-phase current components
PMU	Phasor measurement units
P_{actual}	Actual transmitted real power (MW)
AWT	Adaptive wavelet transform
SIL	Surge impedance loading (MW)
S	SIL utilization/exceedance (%)
$S_{threshold}$	Fixed SIL stability margin (110%)
$S_{threshold,adaptive}$	Adaptive SIL stability limit (%)
DWT	Discrete wavelet transform
Z_s	Surge impedance (Ω)
Z_c	Characteristic impedance of the line (Ω)
R	Series resistance per km (Ω/km)
L	Line inductance per km (H/km)
C	Line capacitance per km (F/km)
G	Shunt conductance per km (S/km)
γ	Propagation constant of the line
ω	Angular frequency (rad/s)
f	Supply frequency (Hz)
Q_c	Reactive power compensation (MVAR)
PF	Power factor
LVF	Load variation factor
E_w	Wavelet energy of disturbance signals

1742, 2026, 1, Downloaded from https://onlinelibrary.wiley.com/doi/10.1155/jece/8676039 by Jimmy Nabende Wanzala - Mbarara Univ of Science and Te , Wiley Online Library on [15/07/2026]. See the Terms and Conditions (https://onlinelibrary.wiley.com/terms-and-conditions) on Wiley Online Library for rules of use; OA articles are governed by the applicable Creative Commons License

Author Contributions

Robert Mugabe designed the system, Michael Robson Atim and Johnes Obungoloch guided and revised the manuscript; Jimmy Nabende Wanzala guided with the simulation.

Acknowledgments

The authors have nothing to report.

Funding

No funding was received for this research.

Disclosure

All authors read and approved the final manuscript for publication.

Ethics Statement

The authors have nothing to report.

Conflicts of Interest

The authors declare no conflicts of interest.

Data Availability Statement

All data used shall be made available upon request.

References

1. M. Arani and D. Kundur, "A User-Centric Approach Toward Resilient Frequency-Regulating Wind Generators," *ACM Transactions on Cyber-Physical Systems* 4, no. 3 (2020): 1–23, https://doi.org/10.1145/3389682.

2. M. Ghiasi, Z. Wang, M. Mehrandezh, H. Alhelou, and N. Ghadimi, "Enhancing Power Grid Stability: Design and Integration of a Fast Bus Tripping System in Protection Relays," *IEEE Transactions on Consumer Electronics* 71, no. 1 (2024): 561–570, https://doi.org/10.1109/TCE.2024.3519389.

3. J. Machowski, Z. Lubosny, J. Bialek, and J. Bumby, *Power System Dynamics: Stability and Control* (John Wiley & Sons, 2020).

4. R. Mugabe, M. R. Atim, J. Obungoloch, and J. N. Wanzala, "Dynamic Transmission Line Modeling and Real-Time Fault Analysis Using ABCD Parameters Enhanced by Equivalent π-model for Accurate Efficiency and Voltage Stability Assessment," *Engineering Research Express* 7, no. 4 (2025): 0453b4, https://doi.org/10.1088/2631-8695/ae2bbe.

5. A. Jha, B. Appasani, A. Ghazali, et al., "Smart Grid Cyber-Physical Systems: Communication Technologies, Standards and Challenges," *Wireless Networks* 27, no. 4 (2021): 2595–2613, https://doi.org/10.1007/s11276-021-02579-1.

6. S. Meraj, S. Yu, M. Rahman, K. Hasan, M. Lipu, and H. Trinh, "Energy Management Schemes, Challenges and Impacts of Emerging Inverter Technology for Renewable Energy Integration Towards Grid Decarbonization," *Journal of Cleaner Production* 405 (2023): 137002, https://doi.org/10.1016/j.jclepro.2023.137002.

7. J. Hossain and H. Pota, "Robust Control for Grid Voltage Stability: High Penetration of Renewable Energy, Power Systems" (2014), https://doi.org/10.1007/978-981-287-116-9.

8. T. Van Cutsem and C. Vournas, *Voltage Stability of Electric Power Systems* (Springer Science and Business Media, 2007).

9. M. Borghei and M. Ghassemi, "Future Transmission Lines With Increased Loadability Through Geometrical Optimized Phase Configurations and Sub-Conductors in the Bundle," in *2020 IEEE Power & Energy Society Innovative Smart Grid Technologies Conference (ISGT)* (New York, NY: IEEE, 2020), 1–5, https://doi.org/10.1109/ISGT45199.2020.9087758.

10. M. Ghassemi, "High Surge Impedance Loading (HSIL) Lines: A Review Identifying Opportunities, Challenges, and Future Research Needs," *IEEE Transactions on Power Delivery* 34, no. 5 (2019): 1909–1924, https://doi.org/10.1109/TPWRD.2019.2910210.

11. R. Isermann, *Fault-Diagnosis Systems: An Introduction From Fault Detection to Fault Tolerance* (Springer Science and Business Media, 2006).

12. P. Yan, A. Abdulkadir, P. P. Luley, et al., "A Comprehensive Survey of Deep Transfer Learning for Anomaly Detection in Industrial Time Series: Methods, Applications, and Directions," *IEEE Access* 12 (2024): 3768–-3789, https://doi.org/10.1109/ACCESS.2023.3349132.

13. M. Abboush, C. Knieke, and A. Rausch, "Intelligent Identification of Simultaneous Faults of Automotive Software Systems Under Noisy and Imbalanced Data Using Ensemble LSTM and Random Forest," *IEEE Access* 11 (2023): 140022–140040, https://doi.org/10.1109/ACCESS.2023.3340865.

14. A. Mahin, S. Islam, F. Ahmed, and M. Hossain, "Measurement and Monitoring of Overhead Transmission Line Sag in Smart Grid," *A Review, IET generation, Transmission and Distribution* 16, no. 1 (2022): 1–18, https://doi.org/10.1049/gtd2.12271.

15. J. Silva, J. López, C. Guzman, N. Arias, M. Rider, and L. da Silva, "An IoT-Based Energy Management System for AC Microgrids With Grid and Security Constraints," *Applied Energy* 337 (2023): 120904, https://doi.org/10.1016/j.apenergy.2023.120904.

16. U. Farooq and R. B. Bass, "Frequency Event Detection and Mitigation in Power Systems: A Systematic Literature Review," *IEEE Access* 10 (2022): 61494–61519, https://doi.org/10.1109/ACCESS.2022.3180349.

17. N. Nafi, K. Ahmed, M. Gregory, and M. Datta, "A Survey of Smart Grid Architectures, Applications, Benefits and Standardization," *Journal of Network and Computer Applications* 76 (2016): 23–36, https://doi.org/10.1016/j.jnca.2016.10.003.

18. P. K. Dash, A. K. Pradhan, and G. Panda, "A Novel Fuzzy Neural Network Based Distance Relaying Scheme," *IEEE Transactions on Power Delivery* 15, no. 3 (2002): 902–907, https://doi.org/10.1109/61.871350.

19. W. He, Y. Zi, B. Chen, F. Wu, and Z. He, "Automatic Fault Feature Extraction of Mechanical Anomaly on Induction Motor Bearing Using Ensemble Super-Wavelet Transform," *Mechanical Systems and Signal Processing* 54 (2015): 457–480, https://doi.org/10.1016/j.ymssp.2014.09.007.

20. K. A. Saleh, A. Hooshyar, E. El-Saadany, and H. Zeineldin, "Protection of High-Voltage DC Grids Using Traveling-Wave Frequency Characteristics," *IEEE Systems Journal* 14, no. 3 (2019): 4284–4295, https://doi.org/10.1109/jsyst.2019.2958811.

21. E. Arafat, B. Porkar, and M. Ghassemi, "Magnetic Field Analysis of Unconventional High Surge Impedance Loading (HSIL) Transmission Lines With Different Subconductor Configurations: Numerical Comparisons and Performance Evaluation," *Magnetism* 5, no. 3 (2025): 20, https://doi.org/10.3390/magnetism5030020.

22. R. Jain, Y. Velaga, K. Prabakar, M. Baggu, and S. Murali, "Modern Trends in Power System Protection for Distribution Grid With High DER Penetration", E-Prime-Advances in Electrical Engineering," *Electronics and Energy* 2 (2022): 100080.

23. Y. Lee and H. Song, "A Reactive Power Compensation Strategy for Voltage Stability Challenges in the Korean Power System With Dynamic Loads," *Sustainability* 11, no. 2 (2019): 326, https://doi.org/10.3390/su11020326.

24. A. Pazderin, I. Zicmane, M. Senyuk, et al., "Directions of Application of Phasor Measurement Units for Control and Monitoring of Modern Power Systems: A State-of-the-Art Review," *Energies* 16, no. 17 (2023): 6203, https://doi.org/10.3390/en16176203.

25. M. Senyuk, S. Beryozkina, M. Safaraliev, et al., "Bulk Power Systems Emergency Control Based on Machine Learning Algorithms and Phasor Measurement Units Data: A Atate-of-the-Art Review," *Energies* 17, no. 4 (2024): 764, https://doi.org/10.3390/en17040764.

26. G. L. Kusic and D. L. Garrison, "Measurement of Transmission Line Parameters From SCADA Data," *IEEE PES Power Systems Conference*

1742, 2026, 1, Downloaded from https://onlinelibrary.wiley.com/doi/10.1155/jece/8676039 by Jimmy Nabende Wanzala - Mbarara Univ of Science and Te , Wiley Online Library on [15/07/2026]. See the Terms and Conditions (https://onlinelibrary.wiley.com/terms-and-conditions) on Wiley Online Library for rules of use; OA articles are governed by the applicable Creative Commons License

and Exposition 1 (2004): 440–445, https://doi.org/10.1109/PSCE.2004.1397479.

27. "IEEE Guide for the Application of Surge Voltage Protective Equipment on AC Rotating Machinery 1000 Volts and Greater," *IEEE Std* (2004): 1–48, https://doi.org/10.1109/IEEESTD.2004.94494.

28. P. Naidoo, D. Muftic, and N. Ijumba, "Investigations Into the Upgrading of Existing HVAC Power Transmission Circuits for Higher Power Transfers Using HVDC Technology," *EEE Power Engineering Society Inaugural Conference and Exposition in Africa* (2005): 139–142, https://doi.org/10.1109/PESAFR.2005.1611802.

29. I. Murugesan, P. Gunasekaran, S. Muthusamy, and P. Ramamoorthi, "A Normalized Haar Wavelet Transformation Based Firefly Optimization Algorithm for Power Transmission Line Fault Detection Problems," *Energy Sources, Part A: Recovery, Utilization, and Environmental Effects* 45, no. 2 (2023): 4965–4981, https://doi.org/10.1080/15567036.2023.2206797.

30. M. H. Haque, "On-Line Monitoring of Maximum Permissible Loading of a Power System Within Voltage Stability Limits," *IEE Proceedings—Generation, Transmission and Distribution* 150, no. 1 (2003): 107–112, https://doi.org/10.1049/ip-gtd:20020682.

31. J. D. Glover, T. J. Overbye, and M. Sarma, *Power System Analysis and Design* (Cengage Learning, 2017).

32. C. Badresiya and A. Deshpande, "Phasor Measurement Unit Based Fault Detection Using Neural Network," in *2023 Second International Conference on Advances in Computational Intelligence and Communication (ICACIC)* (New York, NY: IEEE, 2023), 1–6, https://doi.org/10.1109/ICACIC59454.2023.10435357.

33. S. M. Brahma and A. A. Girgis, "Development of Adaptive Protection Scheme for Distribution Systems With High Penetration of Distributed Generation," *IEEE Transactions on Power Delivery* 19, no. 1 (2004): 56–63, https://doi.org/10.1109/TPWRD.2003.820204.

34. L. Zhang, H. Chen, A. Faris, et al., *Implementation of Synchrophasor-Based Linear State Estimator for Real-Time Operations, Power System Grid Operation Using Synchrophasor Technology* (Springer, 2019), 335–362, https://doi.org/10.1007/978-3-319-89378-5-14.

35. G. Paramo, A. Bretas, and S. Meyn, "Research Trends and Applications of PMUs," *Energies* 15, no. 15 (2022): 5329, https://doi.org/10.3390/en15155329.

36. D. P. Gomes, C. Ozansoy, and A. Ulhaq, "Vegetation High-Impedance Faults' High-Frequency Signatures via Sparse Coding," *IEEE Transactions on Instrumentation and Measurement* 69, no. 7 (2019): 5233–5242, https://doi.org/10.1109/tim.2019.2950822.

37. S. Mahmoud, A. Salem, and K. Robbersmyr, "Robust Self-Augmented Open-Circuit Fault Diagnosis of Three-Level Inverters for EV Powertrains," *IEEE Transactions on Transportation Electrification* (2025).

38. B. Zhang, Z. Hao, and Z. Bo, "New Development in Relay Protection for Smart Grid," *Protection and Control of Modern Power Systems* 1, no. 1 (2016): 14, https://doi.org/10.1186/s41601-016-0025-x.

39. G. Ziegler, *Numerical Distance Protection: Principles and Applications* (John Wiley and Sons, 2011).

40. P. Kundur, 10, no. 1 (2007), 7–11, Power System Stability, Power System Stability and Control.

41. C. W. Taylor, *Power System Voltage Stability* (McGraw-Hil, 1994).

42. V. Ajjarapu, *Computational Techniques for Voltage Stability Assessment and Control* (Springer, 2007).

43. S. Quaia, "Critical Analysis of Line Loadability Constraints," *International Transactions on Electrical Energy Systems* 28, no. 6 (2018): e2552, https://doi.org/10.1002/etep.2552.

44. R. Gutman, P. P. Marchenko, and R. D. Dunlop, "Analytical Development of Loadability Characteristics for EHV and UHV Transmission Lines," *IEEE Transactions on Power Apparatus and Systems* no. 2 (2007): 606–617, https://doi.org/10.1109/tpas.1979.319410.

45. V. Madani, D. Novosel, S. Horowitz, et al., "IEEE PSRC Report on Global Industry Experiences With System Integrity Protection Schemes (SIPS)," *IEEE Transactions on Power Delivery* 25, no. 4 (2010): 2143–2155, https://doi.org/10.1109/tpwrd.2010.2046917.

46. D. Chakravorty, D. Gutschow, X. Zhang, N. Miller, and D. Auty, "Model Considerations for Black Start Studies Using Distributed Energy Resources," in *CIRED 2021-The 26th International Conference and Exhibition on Electricity Distribution* (New York, NY: IEEE, 2021), 1542–-1546, https://doi.org/10.1049/icp.2021.1699.

47. M. Rasheed, "Analyzing Applications and Properties of the Exponential Continuous Distribution in Reliability and Survival Analysis," *Journal of Positive Sciences* 4, no. 5 (2023): 71–79.

48. T. L. Ching and J. Cai, "Accelerated Reliability Testing: From Practice to Theory," *Reliability Analysis and Maintenance Optimization of Complex Systems* (Berlin, Germany: Springer, 2025), 289–314.

49. R. M. Sheldon, *Introduction to Probability Models* (Academic Press, 2014).

50. J. L. Devore, *Probability and Statistics for Engineering and the Sciences*" (Springer, 2008).

51. D. C. Montgomery and G. C. Runger, *Applied Statistics and Probability for Engineers* (John Wiley and Sons, 2019).

52. W. Q. Meeker, L. A. Escobar, and F. G. Pascual, *Statistical Methods for Reliability Data* (John Wiley and Sons, 2021).

53. R. E. Walpole, R. H. Myers, S. L. Myers, and K. Ye, *Probability and Statistics for Engineers and Scientists* (Macmillan, 1993).

54. L. Zhaojun, *Reliability Engineering* (Taylor and Francis, 2012).

55. J. Giri, M. Parashar, R. Avila-Rosales, and D. Wilson, "The Case for Using Wide-Area Monitoring and Control to Improve the Resilience and Capacity of the Electric Power Grid," *Real-Time Stability in Power Systems: Techniques for Early Detection of the Risk of Blackout* (Berlin, Germany: Springer, 2014), 235–278.

56. E. Hossain, R. Perez, A. Nasiri, and S. Padmanaban, "A Comprehensive Review on Constant Power Loads Compensation Techniques," *IEEE Access* 6 (2018): 33285–33305, https://doi.org/10.1109/access.2018.2849065.

57. J. C. Obi, "A Comparative Study of Several Classification Metrics and Their Performances on Data," *World Journal of Advanced Engineering Technology and Sciences* 8, no. 1 (2023): 308–314.

58. A. Tharwat, "Classification Assessment Methods," *Applied Computing and Informatics* 17, no. 1 (2021): 168–192, https://doi.org/10.1016/j.aci.2018.08.003.

APPENDIX A: Computational Steps in the MATLAB/Simulink Implementation

The proposed SIL-based predictive monitoring framework was implemented in MATLAB/Simulink as a structured real-time algorithm executed at each sampling instant. The implementation follows a sequential computational pathway in which measured electrical quantities are processed to evaluate transmission-line loading severity and probabilistic instability risk.

At each time step t, three-phase voltages and currents, $V_{abc}(t)$ and $I_{abc}(t)$, were acquired from the transmission-line model. These signals were used to compute instantaneous active and reactive power, $P(t)$ and $Q(t)$, which formed the primary inputs to the SIL risk assessment block.

The characteristic impedance was calculated using the distributed parameter relationship $Z_c = \sqrt{L/C}$, where L and C denote line inductance and capacitance. The dynamic SIL was then evaluated as $SIL(t) = |V(t)|^2/(|Z_c|)$, establishing the instantaneous theoretical loadability limit of the corridor.

1742, 2026, 1, Downloaded from https://onlinelibrary.wiley.com/doi/10.1155/jece/8676039 by Jimmy Nabende Wanzala - Mbarara Univ of Science and Te , Wiley Online Library on [15/07/2026]. See the Terms and Conditions (https://onlinelibrary.wiley.com/terms-and-conditions) on Wiley Online Library for rules of use; OA articles are governed by the applicable Creative Commons License

Transmission stress was quantified through the SIL utilization index, $S(t) = (P(t)/SIL(t)) \times 100$, which expresses real-time loading as a percentage of the surge impedance boundary.

To account for operating-condition variability, the receiving-end voltage deviation $\Delta V(t)$ was computed relative to the nominal reference, while the reactive compensation term $Q_c(t)$ was evaluated to reflect reactive power balance. These quantities were incorporated into an adaptive loading threshold defined as $S_{\text{thr}}(t) = a + b\Delta V(t) + cQ_c(t)$, where $a = 110$ represents the base SIL security margin, and b and c are sensitivity coefficients modeling voltage and reactive power influence on stability limits.

The exceedance severity was determined as $\Delta S(t) = S(t) - S_{\text{thr}}(t)$. If $\Delta S(t) \leq 0$, the system operated within secure limits. For $\Delta S(t) > 0$, probabilistic instability assessment was activated. Fault likelihood was evaluated using an exponential reliability model, $P_f(t) = 1 - e^{-k\Delta S(t)}$, where k is the calibrated instability growth constant obtained from regression of simulated operating data. This formulation ensures monotonic risk escalation with increasing SIL exceedance.

A predictive fault alert was issued when $P_f(t) > 0.90$, representing a high-confidence instability boundary. All computed indices $SIL(t)$, $S(t)$, $S_{\text{thr}}(t)$, $\Delta S(t)$, and $P_f(t)$ were updated iteratively at each sampling instant and logged for postprocessing and visualization. The resulting architecture forms a continuous real-time monitoring loop suitable for wide-area transmission-line stability assessment.

The full MATLAB script could not be added to the manuscript due to length constraints, but it is available for access at https://drive.google.com/file/d/1ySK2S_-758uy-k4Z0-hYaZ46WQVIVjSb/view?usp=sharing.

APPENDIX B: Accuracy Computation Method

To quantify detection accuracy, simulations comprising 570 representative fault and instability scenarios were conducted within the developed transmission-line monitoring framework. The experimental design incorporated multiple fault categories, fault locations, and loading regimes to ensure comprehensive coverage of realistic transmission-system disturbances. Considered fault types included single line-to-ground (SLG), line-to-line (LL), double line-to-ground (DLG), and three-phase (3-ϕ) faults, each introduced at strategically selected points along the transmission corridor.

To capture system behavior under varying stress conditions, each fault type was simulated across three loading levels: light load ($\leq$ 80% SIL), nominal load ($\approx$ 100% SIL), and heavy load ($\geq$ 120% SIL). Furthermore, repeated simulation runs were executed to account for stochastic variations in fault inception timing and dynamic system response. The resulting experimental matrix yielded a total of 570 simulated events, as summarized in Table A1. All simulations were performed over a 24-h test horizon, representing a complete daily load cycle. This duration enabled the monitoring algorithm to be evaluated under off-peak, ramping, and peak demand intervals, thereby reflecting realistic temporal variations in transmission-line loading and stability conditions.

TABLE A1 | Simulation matrix used to generate representative fault scenarios.

Fault type	Locations	Load levels	Runs per case	Total events
SLG	5	3	10	150
LL	5	3	10	150
DLG	5	3	10	150
3- ϕ	4	3	10	120
Total				570

Detection accuracy was subsequently computed using the standard classification metric defined in Equation (B.1) [57, 58].

$$\text{Accuracy} = \frac{TP + TN}{TP + TN + FP + FN} \times 100\ \%\,, \tag{B.1}$$

where TP, TN, FP, and FN denote true positives, true negatives, false positives, and false negatives, respectively. To evaluate detection performance, each simulated scenario was classified according to the correspondence between the actual system condition and the monitoring algorithm decision. When a fault event occurred and the algorithm correctly issued a predictive alert, the outcome was recorded as a true positive (TP). Conversely, if a fault was present but no alert was generated, the event was categorized as a false negative (FN). Normal operating scenarios correctly identified as nonfault states were recorded as true negatives (TN), while instances in which the algorithm falsely indicated a fault under normal conditions were classified as false positives (FP). The distribution of detection outcomes obtained across the simulated scenarios is summarized in Table A2.

TABLE A2 | Detection outcome distribution across simulated scenarios.

Classification metric	Number of events
True positives (TP)	278
True negatives (TN)	262
False positives (FP)	18
False negatives (FN)	12
Total	570

Using the outcome distribution in Table A2, detection accuracy was computed by substituting the observed values into Equation (B.2).

$$\text{Accuracy} = \frac{278 + 262}{278 + 262 + 18 + 12} \times 100 = 94.74\ \%\,. \tag{B.2}$$

This result indicates that the proposed SIL-based monitoring framework correctly classified transmission-line operating states in over 94% of the evaluated scenarios, demonstrating strong predictive reliability under diverse loading and fault conditions.

APPENDIX C: Simulation Setup and System Configuration

All simulations used a single-circuit three-phase transmission line model connected between a sending-end generator and a receiving-end load. The system represents a typical 220-kV, 200-km overhead transmission line. The distributed-parameter line was modeled using per-unit-length series and shunt impedance components. The transmission line electrical parameters used in the simulation are summarized in Table A3.

TABLE A3 | Transmission line parameters used in simulation.

Nominal line voltage, V_{nominal}	220 kV
Line length, d	200 km
Resistance, R	0.0122 Ω/km
Inductance, L	1.2 mH/km
Capacitance, C	0.009 μ F/km
Conductance, G	3×10^{-6} S/km
Frequency, f	50 Hz
Surge impedance, $Z_s = \sqrt{L/C}$	365 Ω

1742, 2026, 1, Downloaded from https://onlinelibrary.wiley.com/doi/10.1155/jece/8676039 by Jimmy Nabende Wanzala - Mbarara Univ of Science and Te , Wiley Online Library on [15/07/2026]. See the Terms and Conditions (https://onlinelibrary.wiley.com/terms-and-conditions) on Wiley Online Library for rules of use; OA articles are governed by the applicable Creative Commons License

The receiving-end load was modeled using an adjustable three-phase RLC load to generate time-varying loadability conditions. Load imbalance was introduced by modifying the RLC values independently for Phases A, B, and C. Voltage and current were measured at both ends of the transmission line. The simulation used a continuous-time domain with a fixed-step solver (ode23tb), a sampling frequency of 20 kHz, and total simulation horizons of 10 s and 24 h for short-term and long-term stability analyses, respectively.

The detailed internal structures of Figure 2 are presented in Figures A1, A2, A3, and A4.

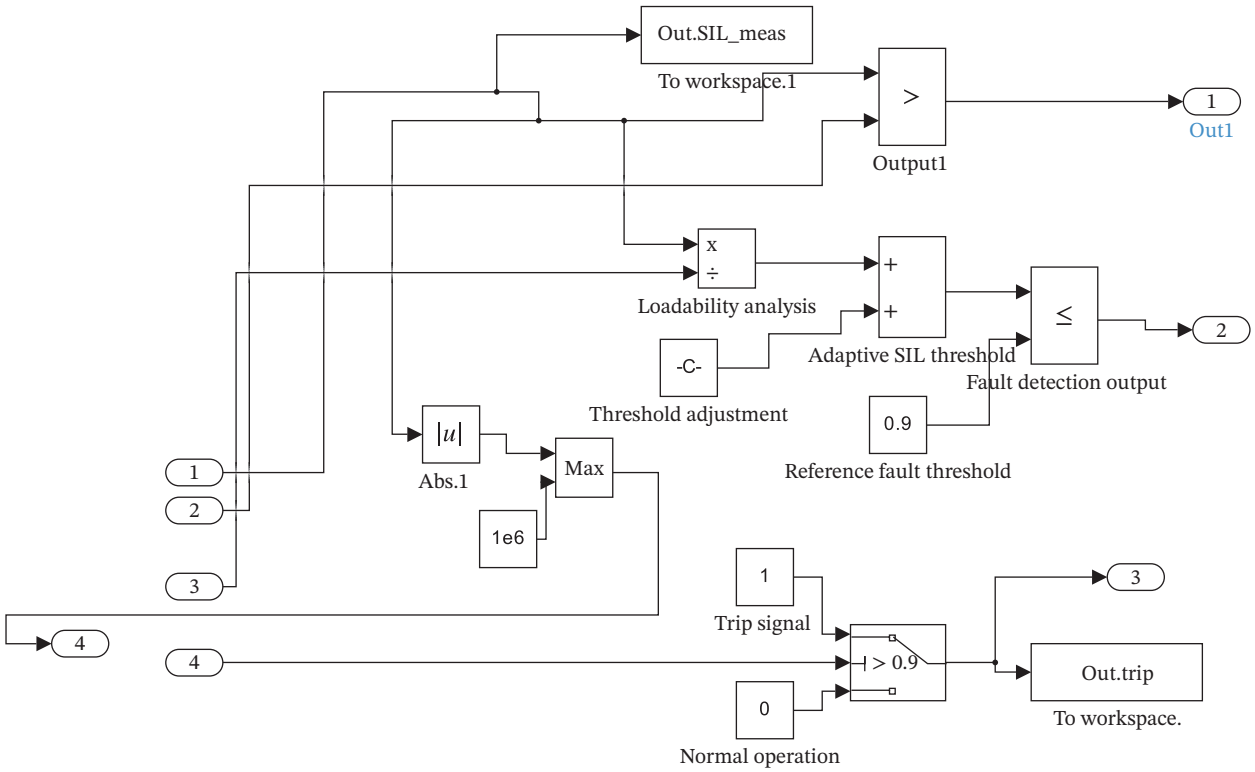


FIGURE A1 | Detailed implementation of the SIL protection logic subsystem.

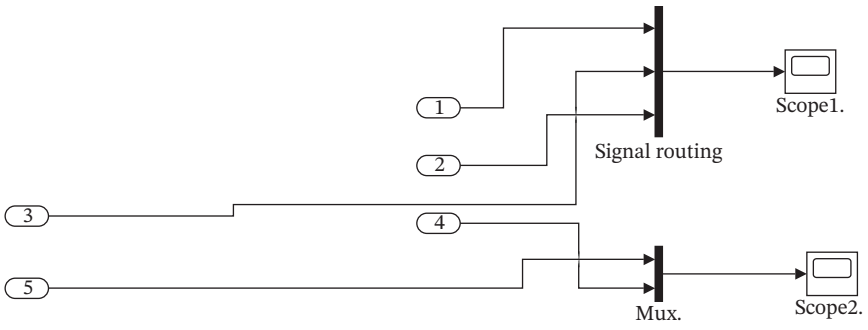


FIGURE A2 | Expanded view of the signal visualization subsystem.

1742, 2026, 1, Downloaded from https://onlinelibrary.wiley.com/doi/10.1155/jece/8676039 by Jimmy Nabende Wanzala - Mbarara Univ of Science and Te , Wiley Online Library on [15/07/2026]. See the Terms and Conditions (https://onlinelibrary.wiley.com/terms-and-conditions) on Wiley Online Library for rules of use; OA articles are governed by the applicable Creative Commons License

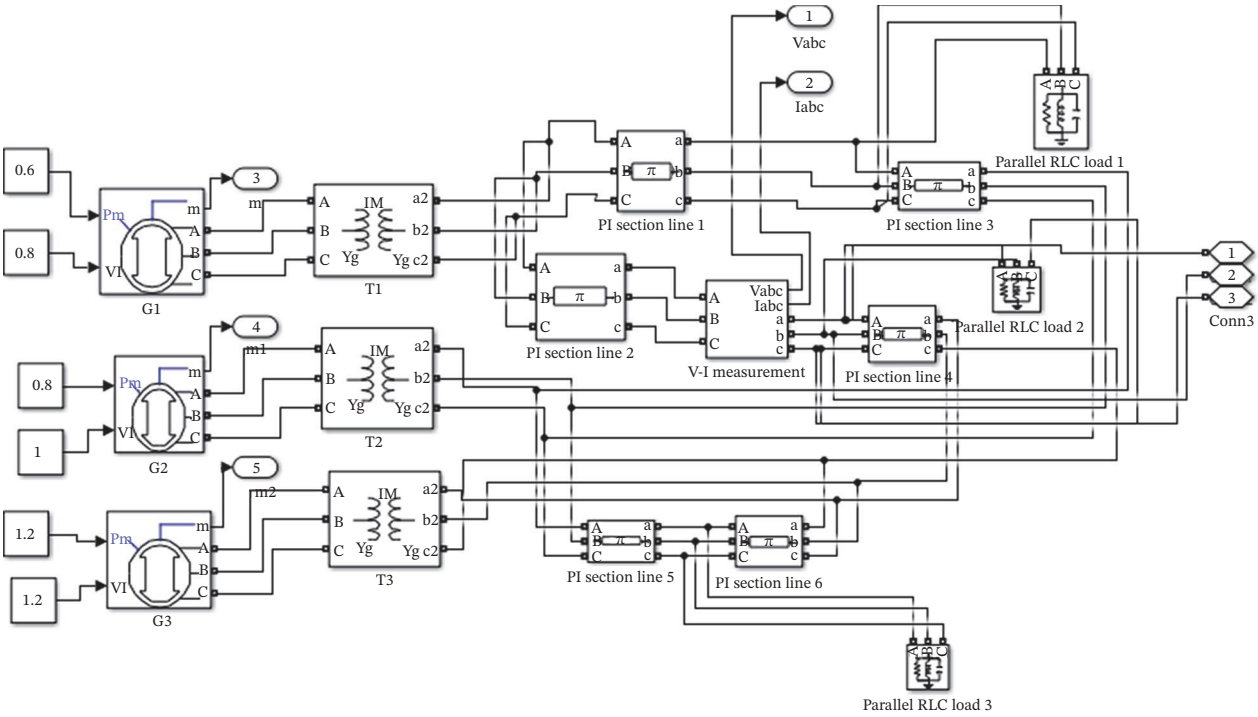


FIGURE A3 | IEEE 9-bus feeder subsystem.

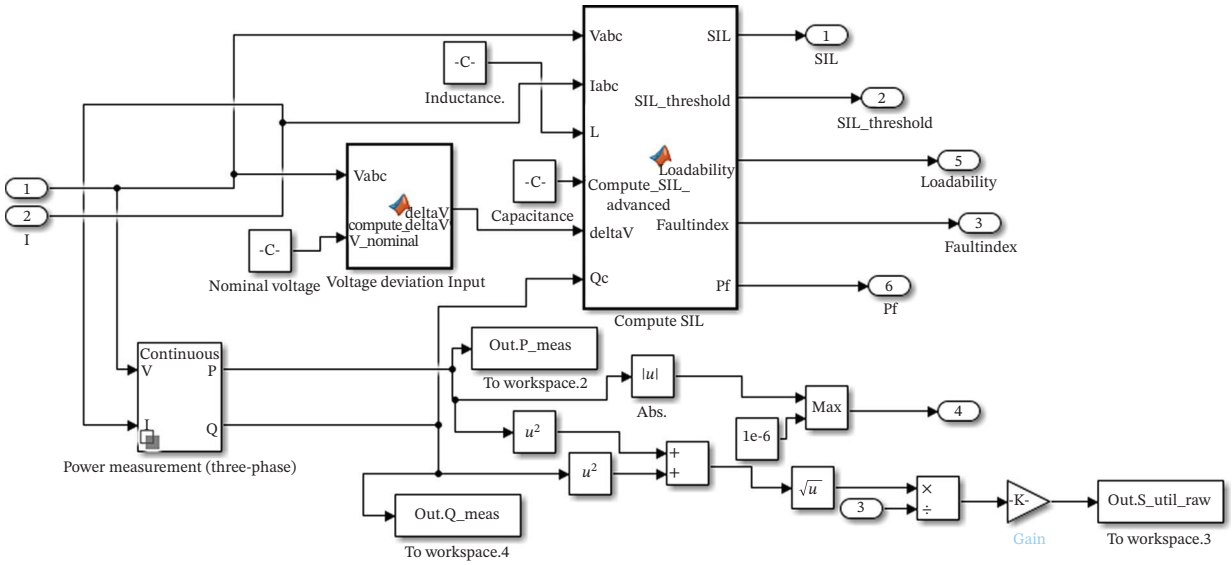


FIGURE A4 | Internal architecture of the SIL risk assessment subsystem, illustrating voltage deviation computation, three-phase power measurement, advanced SIL evaluation, loadability estimation, and probabilistic fault index generation.

1742, 2026, 1, Downloaded from https://onlinelibrary.wiley.com/doi/10.1155/jece/8676039 by Jimmy Nabende Wanzala - Mbarara Univ of Science and Te , Wiley Online Library on [15/07/2026]. See the Terms and Conditions (https://onlinelibrary.wiley.com/terms-and-conditions) on Wiley Online Library for rules of use; OA articles are governed by the applicable Creative Commons License